MNRAS **472,** 1473–1481 (2017)
Advance Access publication 2017 August 16
doi:10.1093/mnras/stx2069

X-ray lags in PDS 456 revealed by *Suzaku* observations

Chia-Ying Chiang,[1★] E. M. Cackett,[1★] A. Zoghbi,[2] A. C. Fabian,[3] E. Kara,[4,5,6] M. L. Parker,[3] C. S. Reynolds[4,6] and D. J. Walton[3]

[1]*Department of Physics and Astronomy, Wayne State University, Detroit, MI 48202, USA*
[2]*Department of Astronomy, The University of Michigan, 500 Church Street, Ann Arbor, MI 48109-1046, USA*
[3]*Institute of Astronomy, University of Cambridge, Madingley Road, Cambridge CB3 0HA, UK*
[4]*Department of Astronomy, University of Maryland, College Park, MD 20742, USA*
[5]*X-ray Astrophysics Laboratory, NASA/Goddard Space Flight Center, Greenbelt, MD 20771, USA*
[6]*Joint Space Science Institute, University of Maryland, College Park, MD 20742, USA*

Accepted 2017 August 8. Received 2017 August 8; in original form 2017 March 23

ABSTRACT

X-ray reverberation lags from the vicinity of supermassive black holes have been detected in almost 30 active galactic nuclei (AGNs). The soft lag, which is the time delay between the hard and soft X-ray light curves, is usually interpreted as the time difference between the direct and reflected emission, but is alternatively suggested to arise from the direct and scattering emission from distant clouds. By analysing the archival *Suzaku* observations totalling an exposure time of ∼770 ks, we discover a soft lag of 10 ± 3.4 ks at 9.58×10^{-6} Hz in the luminous quasar PDS 456, which is the longest soft lag and lowest Fourier frequency reported to date. In this study, we use the maximum likelihood method to deal with non-continuous nature of the *Suzaku* light curves. The result follows the mass–scaling relation for soft lags, which further supports that soft lags originate from the innermost areas of AGNs and hence are best interpreted by the reflection scenario. Spectral analysis has been performed in this work and we find no evidence of clumpy partial-covering absorbers. The spectrum can be explained by a self-consistent relativistic reflection model with warm absorbers, and spectral variations over epochs can be accounted for by the change of the continuum, and of column density and ionization states of the warm absorbers.

Key words: galaxies: Seyfert – X-rays: galaxies.

1 INTRODUCTION

The geometry of an active galactic nucleus (AGN) is widely accepted to be an accretion disc rotating around the central supermassive black hole and illuminated by a hard X-ray source known as the 'corona'. The accretion disc absorbs high-energy photons, and then atomic transitions take place and emit a series of X-ray emission lines in which the Fe Kα line is the most prominent. The fluorescent lines are intrinsically narrow but sometimes appear broad and asymmetric in the observed spectrum. The shape of the broad, skewed Fe Kα emission line discovered in the Type 1 AGN MCG-6-30-15 (Tanaka et al. 1995) can be caused by special and general relativistic effects (Fabian et al. 1989) if the line originates from the innermost part of the accretion disc where strong gravitational fields of the central black hole cast important effects. This provides a powerful method of measuring the inner radius of the accretion disc (and hence the black hole spin in accreting black hole systems) using the iron line profile (see reviews by Miller 2007; Fabian & Ross 2010). Nevertheless, some researchers suggested that the central engine cannot be directly observed even in the X-ray band and proposed a partial-covering scenario to explain the spectral properties of the X-ray spectrum of AGNs (Inoue & Matsumoto 2003; Miller, Turner & Reeves 2009). If this is the case, we cannot obtain information from the innermost areas of black holes via X-ray observations. Thus, the inner radius of the accretion disc cannot be measured and alternative methods need to be developed to probe the vicinity of accreting systems. Risaliti et al. (2013) used simultaneous *XMM–Newton* and *NuSTAR* observations to break spectral degeneracy and found that reflection of NGC 1365 arises from a region within 2.5 gravitational radii ($R_g = GM/c^2$), but it is difficult to distinguish the relativistic reflection model and the partial-covering scenario using spectral analysis in most X-ray observations (Walton et al. 2014). In order to break this degeneracy, detailed spectral-timing analyses have been performed in recent years. The principal goal of these studies have been to search for the reverberation lags predicted by the disc reflection scenario (Fabian et al. 1989; Reynolds et al. 1999).

★ E-mail: ft8320@wayne.edu (C-YC); ecackett@wayne.edu (EMC)

The first significant X-ray reverberation lag was found in the narrow-line Seyfert 1 (NLS1) galaxy 1H0707-495 (Fabian et al. 2009, see McHardy et al. 2007 for an earlier hint in Ark 564). An ∼30 s soft lag, which implies that the soft X-rays lag behind the hard X-rays by 30 s, was reported as evidence supporting the reflection scenario. Similar soft lags have been reported in a number of AGNs as well (Emmanoulopoulos, McHardy & Papadakis 2011; Zoghbi et al. 2012, 2014; Cackett et al. 2013; De Marco et al. 2013; Kara et al. 2013a,c, 2015, 2016). However, alternative explanations of soft lags were proposed. Jin et al. (2013) suggested that the majority of the soft excess in the NLS1 PG 1244+026 is produced by a cool Comptonization component rather than reflection. Gardner & Done (2014) further examined the source and found that a model for the soft excess consisting of intrinsic emission from the accretion flow and reprocessed emission can explain the spectral and timing properties of PG 1244+026. Some works suggested that soft lags are caused by scattering reverberation from distant (tens to hundreds of R_g) material away from the primary X-ray source (Miller et al. 2010; Legg et al. 2012; Turner et al. 2017). These papers suggested that the true signature of reverberation is the low-frequency lags, and the high-frequency lags inferred as reverberation is just phase-wrapping of the low-frequency signal (however, see counter-arguments in Zoghbi, Uttley & Fabian 2011). Kara et al. (2013c) then showed that the lag-energy spectra of these frequency regimes were distinct, demonstrating the need for different physical processes. In addition, Walton et al. (2013b) found a low-frequency lag in NGC 6814 where the spectrum seems to be dominated by only the power-law continuum. Both works argued against the distant reverberation scenario, supporting an inner disc reflection reverberation origin for the high-frequency lags. De Marco et al. (2013) examined a sample of AGN with black hole masses spanning $\sim 10^6$–10^8 $M_\odot$ and found that more massive AGNs have larger soft lags appearing at lower Fourier frequencies. The mass–scaling relation and values of lags indicate that soft lags originate in the innermost areas of AGNs. The discovery of Fe Kα reverberation in NGC 4151 (Zoghbi et al. 2012) and 20 subsequent AGNs (Fabian et al. 2013; Kara et al. 2013a,b,c, 2014, 2015, 2016; Zoghbi et al. 2013a) further supports reverberation from the inner disc (see Uttley et al. 2014 for a detailed review of X-ray reverberation). The self-consistency of the relativistic reflection scenario indicates that X-ray observations provide information from the vicinity of black holes and can help understand the central engines of AGNs.

PDS 456 is a luminous ($L_{\rm bol} = 10^{47}$ erg s^{-1}; Simpson et al. 1999) nearby ($z = 0.184$; Torres et al. 1997), radio-quiet quasar, which is known for powerful disc winds/outflows (Reeves, O'Brien & Ward 2003; Reeves et al. 2009) and rapid X-ray variability (Reeves et al. 2000, 2002). The source was observed several times with major X-ray observatories including *BeppoSAX* (Vignali et al. 2000), *ASCA* (Vignali et al. 2000), *XMM–Newton* (Nardini et al. 2015), *Suzaku* (Reeves et al. 2014) and *NuSTAR*. Vignali et al. (2000) and Reeves et al. (2000) both reported a significant absorption feature at around 8–9 keV rest frame in an early *ASCA* observation. The 2007 *Suzaku* observation further revealed that the feature is likely the blueshifted 6.97 keV iron absorption line at velocities of ∼0.25c (Reeves et al. 2009). The ultrafast outflow (UFO) has been confirmed in later observations as well (Gofford et al. 2014; Reeves et al. 2014; Nardini et al. 2015; Matzeu et al. 2016). UFOs have garnered wide interest because these energetic outflows are capable of contributing to AGN feedback. Nardini et al. (2015) interpreted the broadened Fe Kα emission line with the adjacent absorption feature caused by the UFO in *XMM–Newton*/*NuSATR* observation of PDS 456 as a P-Cygni profile produced by an expanding gaseous envelope. In their analysis they also tested the disc absorption scenario (Gallo & Fabian 2011, 2013), but found that it is not required statistically. Apparent spectral variability can be seen by comparing observations taken at different epochs and different observatories. Some previous work used a partial-covering model to account for most of the spectral variability (Gofford et al. 2014; Nardini et al. 2015; Matzeu et al. 2016). We revisit the long, archival *Suzaku* observations to examine if partial-covering absorbers are required to explain the spectrum. Based on the archival observations, the source shows short-term variability and hence an ideal source for timing analysis. PDS 456 has a high-mass black hole (Log $M_{\rm BH} = 8.91 \pm 0.50$; Zhou & Wang 2005), beyond the mass range of the mass–scaling relation in De Marco et al. (2013). In this work, we use the *Suzaku* observations to examine whether a soft lag(s) can be found in this source, such as in other AGNs with lower masses, and if the result still follows the mass–scaling relation. With the spectral-timing analysis, we re-examine the data to figure out if the relativistic reflection model gives consistent results.

Table 1. Summary of the *Suzaku* observations of PDS 456.

Obs. ID	Start date	Exposure (ks)	Count rate (ct s^{-1})
701056010	2007 Feb. 24	190.6	$(2.7 \pm 0.1) \times 10^{-1}$
705041010	2011 March 16	125.5	$(1.4 \pm 0.1) \times 10^{-1}$
707035010	2013 Feb. 21	182.2	$(6.7 \pm 0.1) \times 10^{-2}$
707035020	2013 March 03	164.8	$(4.4 \pm 0.1) \times 10^{-2}$
707035030	2013 March 08	108.2	$(5.2 \pm 0.1) \times 10^{-2}$

2 DATA REDUCTION

PDS 456 was observed with *Suzaku* in 2007 (Obs ID: 701056010), 2011 (Obs ID: 705041010) and 2013 (Obs IDs: 707035010, 707035020 and 707035030), with good exposure times of ∼190.6, ∼125.5 and ∼455.2 ks, respectively (see Table 1). The X-ray Imaging Spectrometer (XIS) was operated in the normal mode in all observations. The data were reduced using the HEASOFT V6.16 following the Suzaku Data Reduction Guide. We used a circular region with a 150 arcsec radius to extract source spectra and light curves; the same shaped region was used to extract background products in a source-free region. Response files were generated by the XISRESP script. We combined spectra and response files of the front-illuminated (FI) CCD XIS detectors (XIS0 and XIS3) using ADDASCASPEC in FTOOL. Spectra of different Obs IDs of the 2013 observation were combined using ADDASCASPEC as well. The total absorption-corrected 0.5–10.0 keV FI-detectors fluxes are 9.2×10^{-12}, 6.9×10^{-12} and 4.1×10^{-12} erg cm^{-2} s^{-1} for the 2007, 2011 and 2013 observations. We produced 0.3–10.0 keV background-corrected light curves with 1 ks time bin for the XIS0, XIS1 and XIS3 detectors, and combined all of them to form an overall light curve for each observation. The light curves are displayed in Fig. 1 and it can been seen that the source shows variability in all observations.

The Hard X-ray Detector (HXD) was operated in XIS nominal pointing mode in all observations. We extracted the non-X-ray background using the tuned model. The total background was generated using the PIN reduction script HXDPINXBPI, which combines the non-X-ray background and cosmic background automatically. The net count rates are 0.007, 0.001 and 0.003 count s^{-1} in the effective PIN energy band 15.0–45.0 keV, which are 2.0 per cent, 0.8 per cent and 1.1 per cent of the total background count rate. The source was fairly faint in the band during the latter two observations, and only

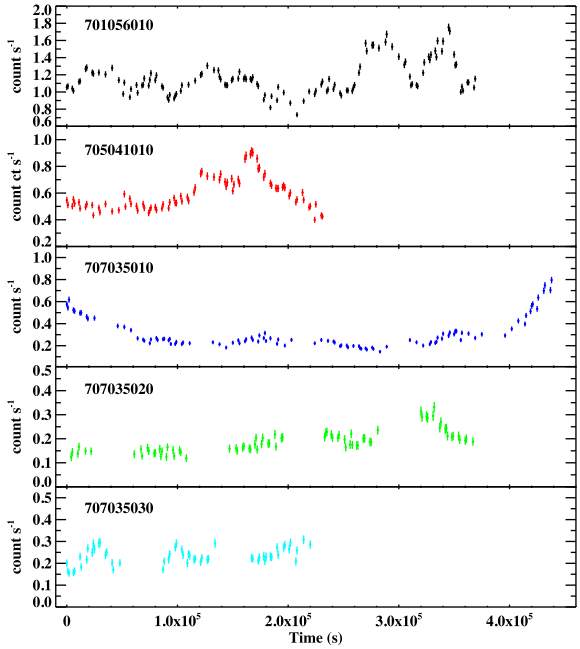

Figure 1. The 0.3–10.0 keV XIS (XIS0, XIS1 and XIS3 combined) light curves for all observations. It can be seen that the duration of the longest observation is ∼438 ks, which is much longer than an *XMM–Newton* orbit (∼130 ks). All the light curves are highly variable.

marginally detected in the 2007 observation. We did not include the PIN light curves in the following timing analysis, and only used the 2007 data for spectral analysis.

3 DATA ANALYSIS

We perform both spectral and timing analyses, described below. Reeves et al. (2009) claimed that a partial-covering Compton-thick absorber is needed to explain the hard excess above 10 keV, while Walton, Reis & Fabian (2010) used a self-consistent, relativistic reflection scenario with a full-covering absorber and successfully interpreted the data. Gofford et al. (2014) and Matzeu et al. (2016) suggested that partial-covering Compton-thick winds are required to interpret the spectral variability shown in PDS 456, though latest work by Matzeu et al. (2017) ruled out partial-covering absorption to be the physical mechanism behind short time-scale variability, as the time-scales are too short to be induced by variable absorption. Since the 2011 and 2013 observations have not been tested using the relativistic reflection model, we include spectral analysis in this work though we mainly focus on timing analysis here.

De Marco et al. (2013) reported a negative lag of ∼400 s at $\sim 3 \times 10^{-5}$ Hz, which was not significantly detected ($<1\sigma$), between the soft (0.3–1 keV) and hard (1–5 keV) energy bands using short *XMM–Newton* observations. Based on the frequency–mass relation of De Marco et al. (2013), the lag of PDS 456 should appear at $\sim 10^{-5}$ Hz and a frequency band including frequencies lower than 10^{-5} Hz needs to be probed to confirm detection. In this work, we use long *Suzaku* observations to probe low Fourier frequencies which *XMM–Newton* data cannot reach. We select the soft and hard bands, which are slightly different from the choice of De Marco et al. (2013), based on results of spectral analysis.

In all the spectral analyses, which were performed using the XSPEC 12.8.2 package (Arnaud 1996), the 'wilm' abundances (Wilms, Allen & McCray 2000) and 'vern' cross-section (Verner et al. 1996) were used. All of the errors quoted in the spectral analysis represent the 90 per cent confidence level, while errors in the timing analysis represent 1σ uncertainties.

3.1 Spectral analysis

We fit the FI XIS spectra in the 0.5–10.0 keV energy range, excluding energies from 1.7–2.1 keV due to known calibration issues. We fit the PIN spectrum over the 15.0–45.0 keV energy band but only the spectrum of the 2007 observation was included. Note that there is mild spectral variability in the 2013 observation. However, in this work we focus on the overall interpretation of the spectrum rather than the variations of warm absorbers, and we use the combined 2013 spectrum for spectral fitting. The data were fit using the same model used in Walton et al. (2013a), which consists of a power law and relativistic disc reflection components and an XSTAR grid (the same one used in Walton et al. 2010, 2013a) to model the absorption feature shown around the Fe K band caused by the ultrafast flow. Galactic absorption was accounted for using the TBABS model in XSPEC. We use the REFLIONX grid (Ross & Fabian 2005) to model reflected emission, and the RELCONV (Dauser et al. 2010) kernel to act on the reflected emission to account for relativistic effects. We assume the inner edge of the accretion disc to extend down to the innermost stable circular orbit (ISCO), and set the outer radius to be 400 R_g ($R_g = GM/c^2$). The iron abundance of the accretion disc and the outflow is set to be identical.

In the spectral fitting we set parameters which are not expected to change significantly over time to be the same in all data. These are the column density of Galactic absorption N_H, the iron abundance A_{Fe}, the spin parameter a^* and the inclination angle i. Reeves et al. (2009) have shown that the UFO is persistent throughout the 2007 and 2011 *Suzaku* observations, with an outflow velocity of 0.25–0.3c. Matzeu et al. (2016) examined the 2013 *Suzaku* observation and found an outflow velocity of $0.25^{+0.01}_{-0.05}c$. Nardini et al. (2015) also reported a similar value of $0.25 \pm 0.01c$ using the long 2013–14 *XMM–Newton* data, implying the UFO in PDS 456 remains at constant velocity across several years. Hence we link the redshift of the XSTAR grid across all data as well. In order to expedite the fitting process, we fit all data together to obtain the best-fitting 'unchanged parameters' mentioned above, and then fit each observation individually with restricting these parameters to vary within the best-fitting error range. We show the best-fitting values of the 'unchanged parameters' in Table 2.

The model results in a good χ^2/d.o.f. of 1131/1107 for the 2007 observation and the best-fitting parameters are shown in Table 2. We obtain χ^2/d.o.f. = 831/788 and 1300/1124 for the 2011 and 2013 data, respectively. It seems there is a mild curvature around 1 keV in the 2013 spectrum (see the second last lower panel in Fig. 2) which causes residuals and the model could not give as good a fit as for the 2007 and 2011 data. The feature could be caused by emission or absorption. We find that the curvature cannot be modelled by a single emission/absorption line nor by an absorption edge. If adding an ionizaed absorber component (ABSORI in XSPEC) in the model, the fitting improves to χ^2/d.o.f. = 1171/1124, implying that the distortion in the 2013 spectrum is caused by a warm absorber. Moreover, Nardini et al. (2015) also identified a fully covered warm absorber that affects the spectrum below <2 keV in the 2013 *XMM–Newton* observation. We generate another XSTAR grid (assuming $\Gamma = 2$) with a lower ionization range (log $\xi = 0.5$–2), to account for the effects of the warm absorber. Note that we set the covering fraction for both the high ionization (to account for the UFO) and low ionization (to model the <2 keV spectrum affected by

Table 2. Parameters for the best-fitting reflection model to the data, in which $N_{\rm H}$ is given in 10^{21} cm^{-2}, and ξ in erg cm s^{-1}. The normalization of the power-law component is expressed in photons keV^{-1} cm^{-2} s^{-1}. The hard upper limit of q is 8, and that of $A_{\rm Fe}$ is 10.

Component	Parameter	2007	2011	2013
TBABS	$N_{\rm H}$ (10^{21} cm^{-2})	2.6 ± 0.2	–	–
XSTAR$_1$ (UFO)	$N_{\rm H}$ (10^{22} cm^{-2})	$4.1^{+1.2}_{-3.0}$	$0.9^{+0.9}_{-0.5}$	$1.8^{+0.8}_{-0.6}$
	Ionization parameter, log ξ	$4.3^{+0.2}_{-0.4}$	$3.5^{+1.0}_{-0.1}$	3.5 ± 0.1
	Redshift, z	$-(9.2^{+0.6}_{-0.5}) \times 10^{-2}$	–	–
XSTAR$_2$ (low-energy)	$N_{\rm H}$ (10^{21} cm^{-2})	–	$3.4^{+1.5}_{-0.9}$	$4.8^{+2.1}_{-1.5}$
	Ionization parameter, log ξ	–	$0.5^{+0.2}$	1.2 ± 0.1
	Redshift, z	–	(0.184)	(0.184)
POWERLAW	Photon index, Γ	2.35 ± 0.01	$2.17^{+0.08}_{-0.06}$	$1.73^{+0.06}_{-0.05}$
	Norm	$(2.2 \pm 0.1) \times 10^{-3}$	$(1.2 \pm 0.1) \times 10^{-3}$	$(3.5^{+0.3}_{-0.2}) \times 10^{-4}$
RELCONV	Emissivity index, q	$2.2^{+0.2}_{-0.1}$	$5.3^{+0.7}_{-0.9}$	$6.1^{+0.4}_{-0.5}$
	Spin parameter, a^*	>0.990	–	–
	Inclination, i (deg)	$(65 \pm 2)^\circ$	–	–
REFLIONX	Iron abundance / solar, $A_{\rm Fe}$	>9.3	–	–
	Ionization parameter, ξ	67^{+19}_{-7}	70^{+30}_{-10}	120^{+30}_{-10}
	Norm	$(1.0 \pm 0.3) \times 10^{-6}$	$(1.9^{+0.9}_{-0.6}) \times 10^{-6}$	$(9.4^{+1.6}_{-1.4}) \times 10^{-7}$
χ^2/d.o.f.		1131/1107	784/786	1168/1122

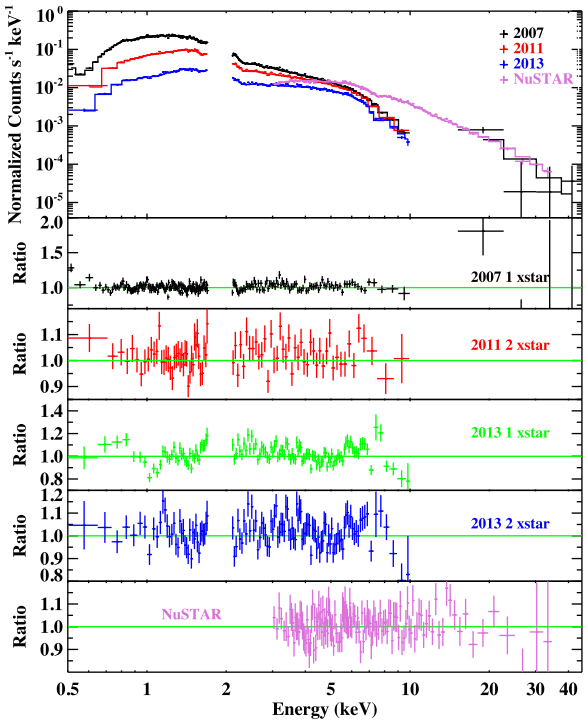

Figure 2. Spectral fits to the *Suzaku* and 2013 *NuSTAR* data of PDS 456 in observed frame. The top panel shows the data used in this work and the lower four panels present the data/model ratios. The 2007 spectrum only requires one XSTAR component to account for the UFO, while the 2011 and 2013 data are better interpreted with an additional low-ionized XSTAR component. We show the fitting result of the 2013 observation, and improvement with the second XSTAR component in different panels. The last panel shows the fitting result of the 2013 *NuSTAR* observation, and it can be seen that the model fits the data very well.

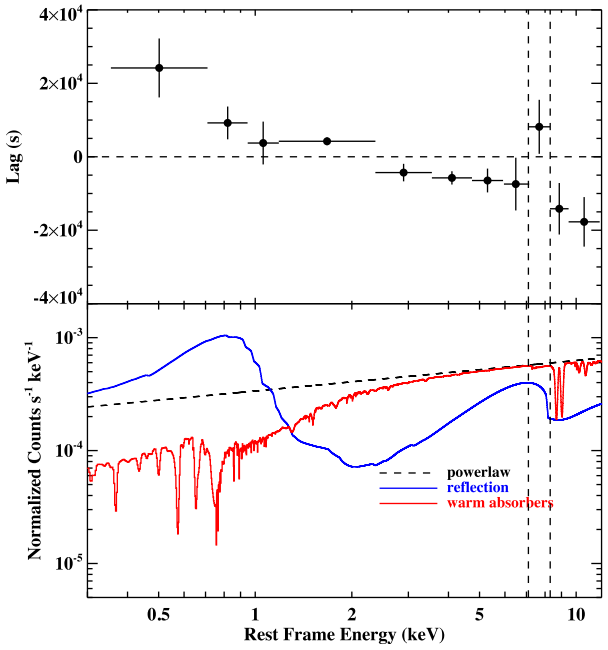

Figure 3. Top: the lag-energy spectrum from all *Suzaku* observations in the [7.2–12.7] $\times$ 10^{-6} Hz frequency range. Bottom: the decomposed best-fitting spectral model of the 2013 *Suzaku* observation in rest frame. The vertical dashed lines are to guide the eye in associating the enhanced lag in the 7.1–8.3 keV band with the blue-wing of the Fe K emission line in the best-fitting model.

warm absorber) XSTAR grids to be 100 per cent (fully covered). The total model is now: TBABS*XSTAR$_1$* XSTAR$_2$*(POWERLAW + RELCONV*REFLIONX). Since there is no resolved absorption lines to constrain the outflow velocity, we fix the redshift of the second XSTAR grid at $z = 0.184$, the redshift of PDS 456. Note that Reeves et al. (2016) reported broad absorption lines at soft X-ray energies and found an outflow velocity of ∼0.1–0.2c. We do not probe the details of the second outflow here as the *Suzaku* XIS data are not good enough to constrain its properties. We find that although the curvature does not seem to appear in the 2011 spectrum, the fitting improves a bit with the low-ionization XSTAR grid. Best-fitting parameters of the model including two XSTAR grids are listed in Table 2 as well. We show the fitting results and decomposed model in Figs 2 and 3. It can be seen that 0.3–0.8 keV is dominated

by reflection and 1–3 keV is primarily contributed by the power-law component. We choose these energy bands as 'soft' and 'hard' bands to perform the timing analysis.

It can be seen that no partial-covering absorbers are included in our model, yet spectral variability can be explained by changes in the continuum and evolution of the warm absorbers. The model fits the 0.5–10 keV energy band well. Wiggles around ∼9 keV in observed frame are likely due to the K β and K edge absorption from Fe XXVI (Nardini et al. 2015). The effective areas of the *Suzaku* XIS detector drop significantly around this band, making detailed modelling difficult. The column density of the high-ionization warm absorber obtained in this work is much lower than that reported in Nardini et al. (2015) ($N_{\rm H} = 6.9^{+0.6}_{-1.2} \times 10^{23}$ cm^{-2}). This might be due to different assumptions made when creating the XSTAR grid and the high iron abundance obtained in this work. In addition, it is known that the UFO evolves slightly over time, and the data they used were not simultaneous with those used in this work. The best-fitting column density of the less-ionized absorber (XSTAR$_2$) is close to that obtained in Nardini et al. (2015), but with a slightly higher ionization parameter ($N_{\rm H} \sim (1.8–4.3) \times 10^{21}$ cm^{-2} and log $\xi = 0.31 \pm 0.02$ in their work). We also test the model on the 2013 *NuSAR* data which was reduced following the same procedures in Nardini et al. (2015), and it fits the 3–35 keV energy band in the observed frame very well (see the last panel of Fig. 2). We obtain a good χ^2/d.o.f. of 348/342, and major parameters (photon index, ionization parameters and column densities of warm absorbers, etc.) are broadly consistent with those reported in Nardini et al. (2015). This indicates that our model can interpret the broad-band NuSTAR data successfully.

We also replace the REFLIONX grid with the XILLVER (Dauser et al. 2010; García et al. 2014) model to test if the results are consistent. We find that major line parameters such as the spin parameter and iron abundance are broadly consistent. The XILLVER model tends to give a higher photon index, a higher emissivity index and a lower ionization parameter, which is likely caused by different assumptions made between these two models. In general, REFLIONX and XILLVER give consistent results to the data.

3.2 Timing analysis

The Fourier phase lag between the hard and soft energy bands can be computed following the technique described in detail in Uttley et al. (2014). In traditional Fourier analysis, continuous light curves are required. However, the technique is not possible with *Suzaku* light curves as the telescope was in a low Earth orbit with an orbital period of ∼5760 s, causing frequent gaps in the data. Although *Suzaku* data cannot be analysed by the traditional Fourier technique, the duration of an observation is around twice its exposure time, making these data ideal to probe the low Fourier frequency domain which is desired when studying massive AGNs. Zoghbi, Reynolds & Cackett (2013b) developed a method to determine the power-spectrum density and lags from non-continuous data, containing gaps. This method uses a maximum likelihood approach to calculate time lags by fitting the light curves directly. It has been shown by Monte Carlo simulations to give the same results as the traditional Fourier method. Details of how uncertainties are estimated can be found in Zoghbi et al. (2013b).

The *XMM–Newton* observations used by De Marco et al. (2013) only have exposures up to ∼90 ks. The longest observation used in this work was of ∼438 ks duration, and we generated the light curves using an 1 ks time bin, leading to a minimum Fourier frequency of $\sim 2.3 \times 10^{-6}$ Hz and a maximum of 5×10^{-4} Hz (the Nyquist frequency). Roughly even logarithmically spaced frequency bins were used and we ensure at least three data points to fall within each frequency bin. In Fig. 4, we show the power spectrum density (PSD) of the soft and hard light curves. Fig. 5 shows the lag-frequency spectrum between the soft (0.3–0.8 keV, dominated by disc reflection, 0.36–0.95 keV in the rest frame) and the hard (1–3 keV, dominated by primary power-law emission, 1.18–3.55 keV in the rest frame) energy bands. The trend that lags switch from negative to positive (the hard flux lags behind the soft) at low frequency has been seen in a number of previous timing studies (Emmanoulopoulos et al. 2011; Zoghbi et al. 2011; De Marco et al. 2013; Kara et al. 2013a,b), and again occurs in the lag-frequency spectrum of PDS 456 though there is only one frequency bin due to the maximum duration of the light curves. We found the maximum negative lag where the soft band lags the hard by 10 000 ± 3400 s to appear at [7.2–12.7] × 10^{-6} Hz (the amplitude of the soft lag and frequency have been corrected for cosmological redshift). Epitropakis & Papadakis (2016) indicated that too few Fourier frequencies within a bin can bias the result, and there are six Fourier frequencies in this bin. We also examine the long 2013–14 *XMM–Newton* data. None the less, the

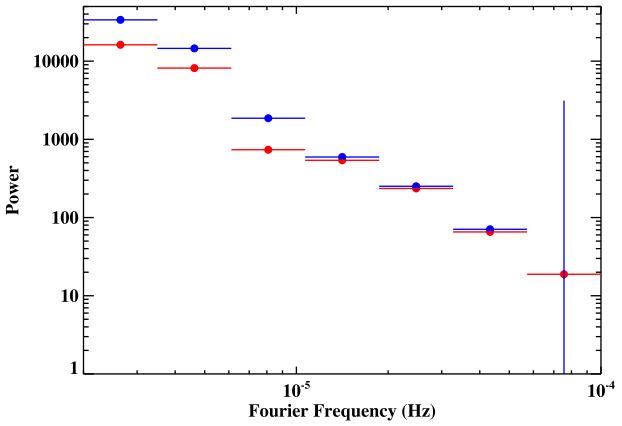

Figure 4. The PSD of the soft (0.3–0.8 keV; 0.36–0.95 keV in the rest frame; red data points) and hard (1–3 keV; 1.18–3.55 keV in the rest frame; blue data points) light curves.

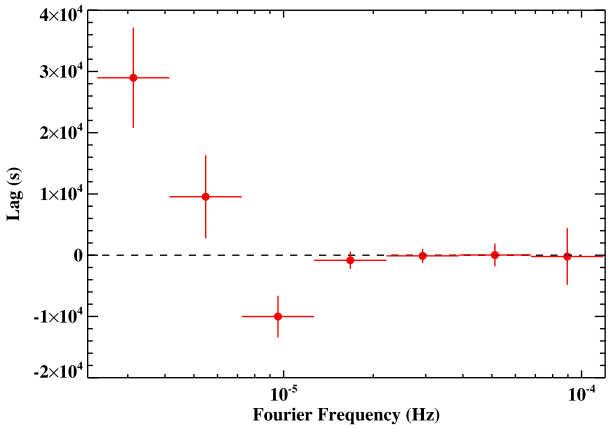

Figure 5. The lag-frequency spectrum computed using ∼770 ks of *Suzaku* data. The lag is calculated between the soft (0.3–0.8 keV; 0.36–0.95 keV in the rest frame) and the hard (1–3 keV; 1.18–3.55 keV in the rest frame) energy bands, and a negative lag means that the soft band lags behind the hard band. It can be seen that the most negative lag is 10 000 ± 3400 s at 9.58×10^{-6} Hz.

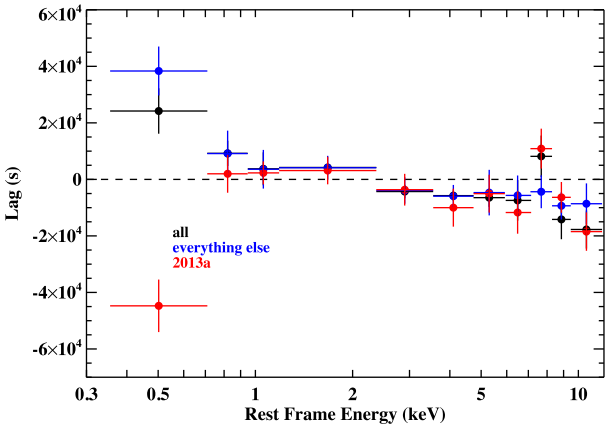

Figure 6. The lag-energy spectrum of *Suzaku* data. The *x*-axis shows energy in rest frame. The spectrum shows the energy dependence of the lags in the frequency range [7.2–12.7] $\times$ 10^{-6} Hz, where the maximum negative soft lag occurs based on the lag-frequency spectrum (Fig. 5). The black points represent results obtained using all data; the red points were calculated using 2013a observation only; the blue points show results obtained using all data except the 2013a observation.

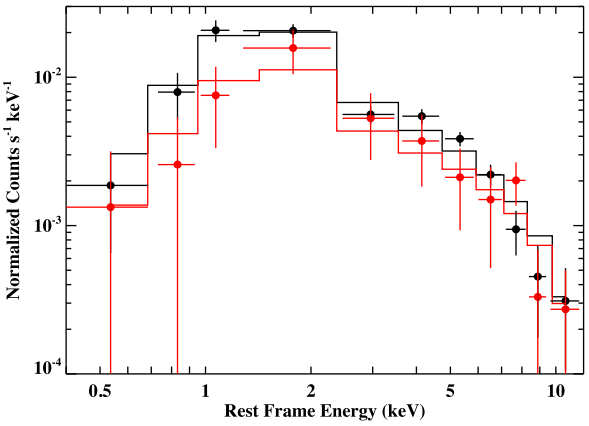

Figure 7. The covariance spectrum for the frequency band [7.2–12.7] $\times$ 10^{-6} Hz. Black points show the overall covariance spectrum and red ones the covariance spectrum of the 2013a (ObsID: 707035010) observation.

longest light curve in that observation is ∼138 ks and there is not enough signal-to-noise ratio to probe the frequency band where the maximum negative lag occurs. We only display results using the *Suzaku* data.

We then take a closer look at the result by generating a lag-energy spectrum to examine how the lag evolves with energy. The lag is calculated between the light curve in each energy bin and the light curve of the reference band. The reference band is the whole energy range (0.3–10 keV) excluding the energy bin of interest. For instance, the reference light curve for the 0.3–0.4 keV band is produced by subtracting the 0.3–0.4 keV light curve from the 0.3–10 keV light curve. The reason to exclude the current band is to ensure the noise remains uncorrelated between the bands (see Zoghbi et al. 2011). Although the choice of reference band would cause the reference light curve to be slightly different for each energy bin, Monte Carlo simulations showed there are only very mild differences (∼1 per cent of systematic error). Figs 3 and 6 show the lag-energy spectrum in the [7.2–12.7] $\times$ 10^{-6} Hz frequency band. The lag begins to have a general negative trend starting at around 3 keV in the rest frame except the 7.1–8.3 keV energy bin. The shape of the lag-energy spectrum is similar to that of IRAS 13224-3809 at high-flux states (Kara et al. 2013b). From looking at the lag-energy spectra from individual observations, we find that the 7.1–8.3 keV bin is dominated by the 2013a observation (see Fig. 6). This energy of this bin lines up with the peak of the Fe K line (see Fig. 6), and may therefore be associated with an Fe K lag, though it cannot be confirmed based on current data. We also note that the lowest energy bin at ∼0.5 keV in the 2013a observation shows a significant difference compared to the average lag-energy spectrum. Changes in the shape of the reflection spectrum (such as the ionization parameter), can cause changes in the lag-energy spectrum (Chainakun & Young 2015; Chainakun, Young & Kara 2016). Moreover, this observation also requires the strongest warm absorber which could affect the lag there (see Discussion).

To investigate the variable spectrum further, we create the covariance spectrum, which is a measure of the absolute amplitude of correlated variations in count rate as a function of energy (Wilkinson & Uttley 2009; Uttley et al. 2014), following the method described in Uttley et al. (2014). The covariance spectrum only picks out the correlated variations and allows direct comparison with the time-averaged spectrum. Fig. 7 shows the covariance spectrum of the [7.2–12.7] $\times$ 10^{-6} Hz frequency band, where the soft lag is detected. Notably, the covariance spectrum of the 2013a observation shows an enhancement at the same energy as the tentative Fe K lag. Overall, the covariance spectrum roughly follows a power law with $\Gamma = 1.73$, though there are clear deviations from it.

4 DISCUSSION

The spectrum of PDS 456 can be simply explained by relativistic reflection with two full-covering absorbers, where one is associated with the UFO and the other related to another warm absorber with a lower ionization state and a lower outflow speed which cannot be tested by the *Suzaku* data. We do not find any partial-covering absorbers that are required to interpret the data. The change in the continuum, the column density and ionization state of the warm absorbers are sufficient to explain the spectral variability between observations.

We find a soft lag of 10 000 $\pm$ 3400 s at 9.58 $\times$ 10^{-6} Hz via the maximum likelihood method, which is the largest soft lag and the lowest frequency to date in X-ray reverberation studies. Previous works do not probe Fourier frequencies below 10^{-5} Hz because there are no continuous light curves that are long enough to reach the low-frequency domain. We will compare the results with previous literature in the following.

4.1 Mass-scaling relation

We first compare our result with those obtained in De Marco et al. (2013). In Fig. 8, we present the result of PDS 456 using a red triangle data point. It can be seen that PDS 456 lies close to the extrapolated relation obtained by De Marco et al. (2013). The data point of PDS 456 is slightly above the mass–scaling relation, which could be explained by the tentative correlation between lag and Eddington ratio (Kara et al. 2016). PDS 456 is claimed to be accreting at Eddington or above and it is not surprising that it is slightly away from the relation. In fact, the light travel distance converting from the amplitude of the soft lag is within 3 R_g (see the red dash line in Fig. 8), which is as small as values found in other AGNs (1–10 R_g). Previous work of De Marco et al. (2013) only probe Fourier frequency in the range of 10^{-5} to 10^{-3} Hz and AGNs with lower masses due to the use of continuous *XMM–Newton*

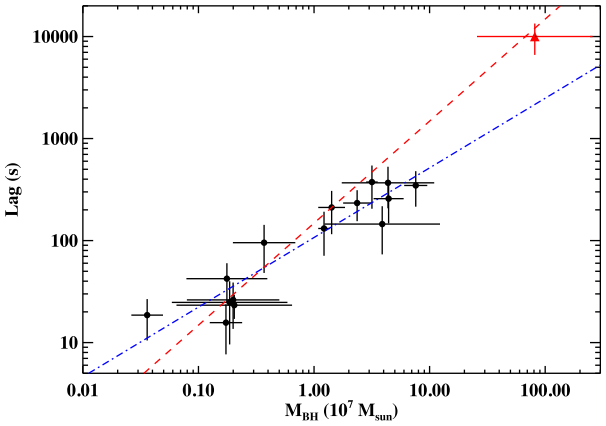

Figure 8. Lag versus black hole mass–scaling relation from De Marco et al. 2013 (black). The *y*-axis shows the most significant soft lags detected in AGNs. The red triangle on top represents the data point of PDS 456 measured in this work. The blue dot–dashed line is drawn using the best-fitting relation of data from De Marco et al. (2013). The red dash line presents the light-crossing time at 3 R_g as a function of mass.

observations. The data point of PDS 456 may deviate from the extrapolated best-fitting relation because of potential biases in the De Marco et al. (2013) sample. The maximum length of the *XMM–Newton* light curves biases against finding large soft lags in massive black holes, potentially flattening the relation. Our result shows that the massive quasar PDS 456 follows the mass–scaling relation as well. Lags of sources in the De Marco sample and PDS 456 all imply that these signals are from areas very close to central black holes. Although it is not known if all massive AGNs follow the trend, the result of PDS 456 further supports the hypothesis that soft lags originate from the innermost areas of AGNs.

4.2 Modelling the Fe Kα lag

To better understand the expected Fe Kα reverberation lag in the frequency range [7.2–12.7] $\times 10^{-6}$ Hz, we use the models described in Cackett et al. (2014) to calculate the transfer function for a point source at some height, h, above the black hole. The best-fitting spectral parameters indicate an inclination of 65° and a near maximally spinning black hole. We therefore calculate the transfer function assuming $i = 65°$ and $a = 0.998$. We also assume $h = 10$ GM/c^2, close to what was found for NGC 4151 in Cackett et al. (2014). The spectral fits also indicate a reflection fraction (reflection flux/power flux) of approximately 0.6 at the peak of the iron line in the 2013 observations (it is lower in the other observations). Furthermore, we assume $\log M = 8.91$ (Zhou & Wang 2005).

The aim here is not to fit the data, but just to explore what might be expected to be observed. With the parameters given above we produce the lag-energy spectrum at the frequency of the soft lag in Fig. 9. The lag-frequency spectrum for the energy-averaged iron line is also shown. From the lag-frequency spectrum, we see that for such a massive black hole the frequency range [7.2–12.7] $\times 10^{-6}$ Hz is right where phase wrapping occurs. This means that we expect to see only reverberation from the regions of the disc with the shortest path length differences. With a high inclination angle of 65°, this will be close to the black hole on the near-side of the accretion disc. We therefore expect to see lags from only the most redshifted and blueshifted parts of the line (see Cackett et al. 2014 for detailed descriptions). What is striking about the resultant lag-energy spectrum in Fig. 9 is the narrow peak in the lags in the 7–8 keV range, coming from the most blueshifted emission. The general shape of the lag-energy spectrum is very similar to what is observed in PDS 456 – a peak only in the ∼7–8 keV range and much smaller lags, with little energy-dependence, elsewhere.

We have not calculated a grid of models covering a range of parameters in order to fit the data properly. We do note, however, that given how the frequency range is right where the phase wrapping crosses zero, small changes in the assumed mass, height and inclination can have a big effect on the lag-energy spectrum. If the height of the corona changes with flux (as suggested by spectral fitting, e.g. Fabian et al. 2012) then this could explain why only the 2013a observation shows a significant lag in the 7.1–8.3 keV range.

4.3 Influence of the outflow

Emmanoulopoulos et al. (2011) carried out timing analysis on MCG-6-30-15 using the 0.5–1.5 keV and 2–4 keV light curves. The 0.5–1.5 keV energy band of MCG-6-30-15 is seriously modified by warm absorbers (Chiang & Fabian 2011) and the soft lag obtained from the data might be caused by scattering/absorbing material. Nevertheless, Emmanoulopoulos et al. (2011) found that the soft lag of MCG-6-30-15 is most likely caused by reflection by testing various models. Reverberation lags can still be detected

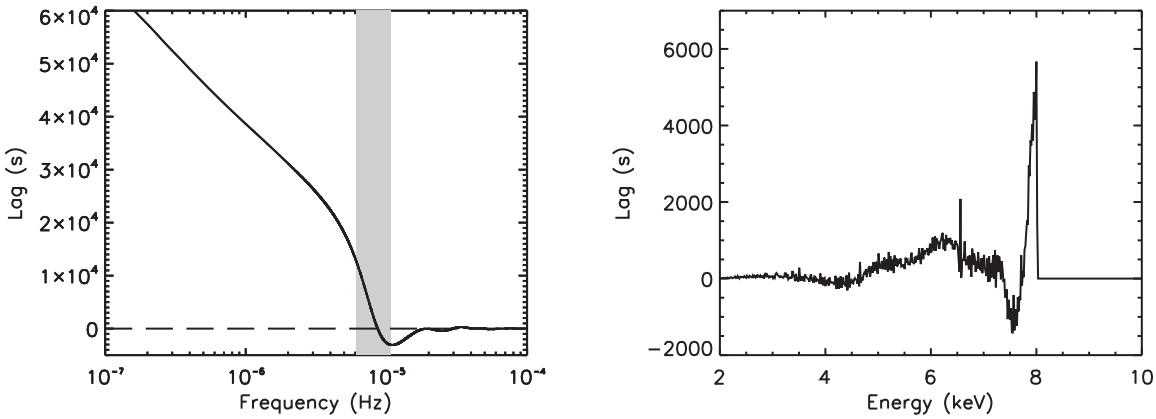

Figure 9. Left: the lag-frequency spectrum for the energy-averaged iron line, assuming $i = 65°$, $h = 10\,GM/c^2$, $a = 0.998$ and $\log M = 8.91$. The grey shaded region shows the frequency range where the soft lag is detected in PDS 456, and over which the lag-energy spectrum (right-hand panel) is calculated. Right: the lag-energy spectrum over the frequency-range [7.2–12.7] $\times 10^{-6}$ Hz, assuming a reflection fraction of 0.6, and parameters listed previously.

even when the timing analysis involves energy bands which are strongly affected by warm absorbers, but strong absorption does inhibit the measurement of time lags. Silva, Uttley & Costantini (2016) investigated data of NGC 4051 and found that warm absorbers do produce time lags in the order of ∼50 s or more at lower frequencies, which is of a longer time-scale than the reverberation lags in NGC 4051 and hence does not pollute the measurement. The time delay is related to the response of the gas to changes in the ionizing continuum and is dependent on the density of the warm absorber. However, only warm absorbers within a certain distance (10^{15} cm to $10^{16.5}$ cm in the case of NGC 4051, ∼3900–123 000 R_g) matter. Those close to the ionizing source respond immediately and gas further out is unable to respond to create a visible time delay. In NGC 4051, the component with a mild ionization parameter of $\log \xi \sim 2.9$ and $N_H = (1.2 \pm 0.2) \times 10^{21}$ cm^{-2} contributed the majority of the soft lag, while the highly ionized ($\log \xi \sim 3.7$) and the least ionized ($\log \xi \sim 0.4$) components cause little differences. The warm absorbers found in PDS 456 are the same type which contributes least in NGC 4051, but column densities are higher than those found in NGC 4051. Assuming that the position of warm absorbers scale with black hole masses, those in PDS 456 should not produce negative lags which coincide with reverberation lags. None the less, detailed analysis is still required to completely rule out the possibility that the time lag detected in PDS 456 is partly produced by variable warm absorbers, as these outflows are complex and can be case dependent.

Kara et al. (2016) examined a sample of Seyfert galaxies, including bare and partially obscured sources, and found ∼50 per cent of them exhibit iron K reverberation. An iron K lag was not detected in some sources with complex absorption such as MCG-6-30-15, but seen in several sources with warm absorbers. IRAS 13224-3809, which is known to have UFO appearing at the iron K band (Parker et al. 2017), does reveal an iron K lag. The presence of warm absorbers does not seem to destroy iron K lags. Warm absorbers do not seem to leave signatures in the lag-energy spectrum (Fig. 6) of PDS 456. The negative trend is disrupted by the 7.1–8.3 keV energy bin in rest frame, where neither of the warm absorbers would affect significantly (the UFO locates at 8–9 keV rest frame, and the second warm absorber casts effects on low-energy band as seen in Fig. 3). None the less, the 7.1–8.3 keV positive lag cannot be confirmed as an iron K lag either. Without enough evidence, the X-ray lag shown in PDS 456 cannot be concluded to be reverberation lag.

Kara et al. (2015) showed that the iron K reverberation lag cannot be found in NGC 1365 in orbits that are highly obscured. They also found a low-frequency soft lag (instead of hard lag as found in other AGNs) in a less-absorbed orbit, which can be explained as a transient phenomenon. There is evidence of a neutral eclipsing cloud in NGC 1365, and the low-frequency soft lag is caused by a change in column density, which can be interpreted as the eclipsing cloud moving out the line of sight. In the case of PDS 456, Matzeu et al. (2016) reported significant short-term X-ray spectral variability on time-scales of ∼100 ks in the 2013 observation, and suggested that the spectral variability can be accounted for by variable covering of the clumpy absorbing gas along the line of sight. If this is true, we should be able to see signatures in the lag-frequency spectrum of the 2013 observation. The lag-frequency spectrum from the combined 2013 observation shows no significant difference from Fig. 5. However, we do see that when looking only at the 2013a lag-energy spectrum in the $[7.2–12.7] \times 10^{-6}$ Hz frequency range, there is a change in the lag in the lowest energy bin (which would be affected most by neutral absorption). But, the lag changes in the opposite sense from what would be expected by the presence of an eclipsing cloud with high column density in PDS 456 during that observation only. This does not reject the possibility of partial-covering Compton-thick absorbers, which could be located further from the centre and do not cast effects on lag measurement. However, recent X-ray microlensing studies have shown that the X-ray emitting region of quasars is compact (less than ∼10 gravitational radii R_g, Dai et al. 2010; Chartas et al. 2012). If clumpy partial-covering absorbers are not in the innermost regions of AGNs, they are more likely to fully cover the source. We have already shown in Section 3.1 that a simple relativistic reflection model with Compton-thin, fully covered warm absorbers can interpret the spectrum of PDS 456 without difficulty. In the timing analysis, we find no evidence to contradict the model.

Based on this work, we did not find evidence for a high-column eclipsing cloud such as that found in NGC 1365 to be present in PDS 456. Although warm absorbers can affect the lag measurement, those with low column density do not seem to contribute significantly to timing analysis. Combining both spectral and timing analyses, the time lag in PDS 456 is more likely to be an X-ray reverberation lag. Nevertheless, given that there is only tentative evidence of an iron K lag, the possibility that the time lag was generated by warm absorbers cannot be completely ruled out.

5 CONCLUSIONS

We present both the spectral and timing analysis of PDS 456 using ∼770 ks of archival *Suzaku* data. We find that the spectrum can be simply explained by relativistic reflection with two full-covering warm absorbers. One of them is the persistent, highly ionized UFO; the other is less ionized and started to appear in the 2011 observation. No partial-covering absorbers were required to interpret spectral variability, and we did not find effects caused by these absorbers in the lag-frequency spectrum either. Based on the spectral analysis, PDS 456 harbours a rapidly spinning black hole of $a^* > 0.99$. Furthermore, we find a soft lag of $10\,000 \pm 3400$ s at 9.58×10^{-6} Hz, which matches the scaling relation and indicates an origin within 3 R_g. More data are required to confirm the relation for massive AGNs with $M > 10^8$ M$_\odot$, but our result further supports the scenario that soft lags originate from the innermost regions of AGNs. The results show that the relativistic reflection model is self-consistent and reveal the robustness of probing areas near the central engine using this model.

ACKNOWLEDGEMENTS

This work was greatly expedited thanks to the help of Jeremy Sanders in optimizing the various convolution models. We thank Phil Uttley for useful discussions. EMC gratefully acknowledges support from the NSF through CAREER award number AST-1351222. CSR thanks NASA for support under grant NNX15AU54G. ACF acknowledges ERC Advanced Grant 340442.

REFERENCES

Arnaud K. A., 1996, in Jacoby G. H., Barnes J., eds, ASP Conf. Ser. Vol. 101, Astronomical Data Analysis Software and Systems V. Astron. Soc. Pac., San Francisco, p. 17

Cackett E. M., Fabian A. C., Zogbhi A., Kara E., Reynolds C., Uttley P., 2013, ApJ, 764, L9

Cackett E. M., Zoghbi A., Reynolds C., Fabian A. C., Kara E., Uttley P., Wilkins D. R., 2014, MNRAS, 438, 2980

Chainakun P., Young A. J., 2015, MNRAS, 452, 333

Chainakun P., Young A. J., Kara E., 2016, MNRAS, 460, 3076
Chartas G., Kochanek C. S., Dai X., Moore D., Mosquera A. M., Blackburne J. A., 2012, ApJ, 757, 137
Chiang C.-Y., Fabian A. C., 2011, MNRAS, 414, 2345
Dai X., Kochanek C. S., Chartas G., Kozłowski S., Morgan C. W., Garmire G., Agol E., 2010, ApJ, 709, 278
Dauser T., Wilms J., Reynolds C. S., Brenneman L. W., 2010, MNRAS, 409, 1534
De Marco B., Ponti G., Cappi M., Dadina M., Uttley P., Cackett E. M., Fabian A. C., Miniutti G., 2013, MNRAS, 431, 2441
Emmanoulopoulos D., McHardy I. M., Papadakis I. E., 2011, MNRAS, 416, L94
Epitropakis A., Papadakis I. E., 2016, A&A, 591, A113
Fabian A. C., Ross R. R., 2010, Space Sci. Rev., 157, 167
Fabian A. C., Rees M. J., Stella L., White N. E., 1989, MNRAS, 238, 729
Fabian A. C. et al., 2009, Nature, 459, 540
Fabian A. C. et al., 2012, MNRAS, 419, 116
Fabian A. C. et al., 2013, MNRAS, 429, 2917
Gallo L. C., Fabian A. C., 2011, MNRAS, 418, L59
Gallo L. C., Fabian A. C., 2013, MNRAS, 434, L66
García J. et al., 2014, ApJ, 782, 76
Gardner E., Done C., 2014, MNRAS, 442, 2456
Gofford J. et al., 2014, ApJ, 784, 77
Inoue H., Matsumoto C., 2003, PASJ, 55, 625
Jin C., Done C., Middleton M., Ward M., 2013, MNRAS, 436, 3173
Kara E., Fabian A. C., Cackett E. M., Steiner J. F., Uttley P., Wilkins D. R., Zoghbi A., 2013a, MNRAS, 428, 2795
Kara E., Fabian A. C., Cackett E. M., Miniutti G., Uttley P., 2013b, MNRAS, 430, 1408
Kara E., Fabian A. C., Cackett E. M., Uttley P., Wilkins D. R., Zoghbi A., 2013c, MNRAS, 434, 1129
Kara E., Cackett E. M., Fabian A. C., Reynolds C., Uttley P., 2014, MNRAS, 439, L26
Kara E. et al., 2015, MNRAS, 446, 737
Kara E., Alston W. N., Fabian A. C., Cackett E. M., Uttley P., Reynolds C. S., Zoghbi A., 2016, MNRAS, 462, 511
Legg E., Miller L., Turner T. J., Giustini M., Reeves J. N., Kraemer S. B., 2012, ApJ, 760, 73
McHardy I. M., Arévalo P., Uttley P., Papadakis I. E., Summons D. P., Brinkmann W., Page M. J., 2007, MNRAS, 382, 985
Matzeu G. A., Reeves J. N., Nardini E., Braito V., Costa M. T., Tombesi F., Gofford J., 2016, MNRAS, 458, 1311
Matzeu G. A., Reeves J. N., Nardini E., Braito V., Turner T. J., Costa M. T., 2017, MNRAS, 465, 2804
Miller J. M., 2007, ARA&A, 45, 441
Miller L., Turner T. J., Reeves J. N., 2009, MNRAS, 399, L69
Miller L., Turner T. J., Reeves J. N., Braito V., 2010, MNRAS, 408, 1928
Nardini E. et al., 2015, Science, 347, 860
Parker M. L. et al., 2017, Nature, 543, 83
Reeves J. N., O'Brien P. T., Vaughan S., Law-Green D., Ward M., Simpson C., Pounds K. A., Edelson R., 2000, MNRAS, 312, L17
Reeves J. N., Wynn G., O'Brien P. T., Pounds K. A., 2002, MNRAS, 336, L56
Reeves J. N., O'Brien P. T., Ward M. J., 2003, ApJ, 593, L65
Reeves J. N. et al., 2009, ApJ, 701, 493
Reeves J. N. et al., 2014, ApJ, 780, 45
Reeves J. N., Braito V., Nardini E., Behar E., O'Brien P. T., Tombesi F., Turner T. J., Costa M. T., 2016, ApJ, 824, 20
Reynolds C. S., Young A. J., Begelman M. C., Fabian A. C., 1999, ApJ, 514, 164
Risaliti G. et al., 2013, Nature, 494, 449
Ross R. R., Fabian A. C., 2005, MNRAS, 358, 211
Silva C. V., Uttley P., Costantini E., 2016, A&A, 596, A79
Simpson C., Ward M., O'Brien P., Reeves J., 1999, MNRAS, 303, L23
Tanaka Y. et al., 1995, Nature, 375, 659
Torres C. A. O., Quast G. R., Coziol R., Jablonski F., de la Reza R., Lépine J. R. D., Gregório-Hetem J., 1997, ApJ, 488, L19
Turner T. J., Miller L., Reeves J. N., Braito V., 2017, MNRAS, 467, 3924
Uttley P., Cackett E. M., Fabian A. C., Kara E., Wilkins D. R., 2014, A&AR, 22, 72
Verner D. A., Ferland G. J., Korista K. T., Yakovlev D. G., 1996, ApJ, 465, 487
Vignali C., Comastri A., Nicastro F., Matt G., Fiore F., Palumbo G. G. C., 2000, A&A, 362, 69
Walton D. J., Reis R. C., Fabian A. C., 2010, MNRAS, 408, 601
Walton D. J., Nardini E., Fabian A. C., Gallo L. C., Reis R. C., 2013a, MNRAS, 428, 2901
Walton D. J. et al., 2013b, ApJ, 777, L23
Walton D. J. et al., 2014, ApJ, 788, 76
Wilkinson T., Uttley P., 2009, MNRAS, 397, 666
Wilms J., Allen A., McCray R., 2000, ApJ, 542, 914
Zhou X.-L., Wang J.-M., 2005, ApJ, 618, L83
Zoghbi A., Uttley P., Fabian A. C., 2011, MNRAS, 412, 59
Zoghbi A., Fabian A. C., Reynolds C. S., Cackett E. M., 2012, MNRAS, 422, 129
Zoghbi A., Reynolds C., Cackett E. M., Miniutti G., Kara E., Fabian A. C., 2013a, ApJ, 767, 121
Zoghbi A., Reynolds C., Cackett E. M., 2013b, ApJ, 777, 24
Zoghbi A. et al., 2014, ApJ, 789, 56

This paper has been typeset from a TEX/LATEX file prepared by the author.